Inorganic Chemistry

pubs.acs.org/IC

Article

Polymorph of $LiAlP_2O_7$: Combined Computational, Synthetic, Crystallographic, and Ionic Conductivity Study

Elvis Shoko,[†] Yun Dang,[†] Guopeng Han, Benjamin B. Duff, Matthew S. Dyer, Luke M. Daniels, Ruiyong Chen, Frédéric Blanc, John B. Claridge, and Matthew J. Rosseinsky*

Cite This: https://doi.org/10.1021/acs.inorgchem.1c01396

Read Online

ACCESS | Metrics & More | Article Recommendations | Supporting Information

ABSTRACT: We report a new polymorph of lithium aluminum pyrophosphate, $LiAlP_2O_7$, discovered through a computationally guided synthetic exploration of the Li−Mg−Al−P−O phase field. The new polymorph formed at 973 K, and the crystal structure, solved by single-crystal X-ray diffraction, adopts the orthorhombic space group *Cmcm* with a = 5.1140(9) Å, b = 8.2042(13) Å, c = 11.565(3) Å, and V = 485.22(17) Å^3. It has a three-dimensional framework structure that is different from that found in other $LiM^{III}P_2O_7$ materials. It transforms to the known monoclinic form (space group $P2_1$) above ~1023 K. Density functional theory (DFT) calculations show that the new polymorph is the most stable low-temperature structure for this composition among the seven known structure types in the $A^IM^{III}P_2O_7$ (A = alkali metal) families. Although the bulk Li-ion conductivity is low, as determined from alternating-current impedance spectroscopy and variable-temperature static ^{7}Li NMR spectra, a detailed analysis of the topologies of all seven structure types through bond-valence-sum mapping suggests a potential avenue for enhancing the conductivity. The new polymorph exhibits long (>4 Å) Li−Li distances, no Li vacancies, and an absence of Li pathways in the c direction, features that could contribute to the observed low Li-ion conductivity. In contrast, we found favorable Li-site topologies that could support long-range Li migration for two structure types with modest DFT total energies relative to the new polymorph. These promising structure types could possibly be accessed from innovative doping of the new polymorph.

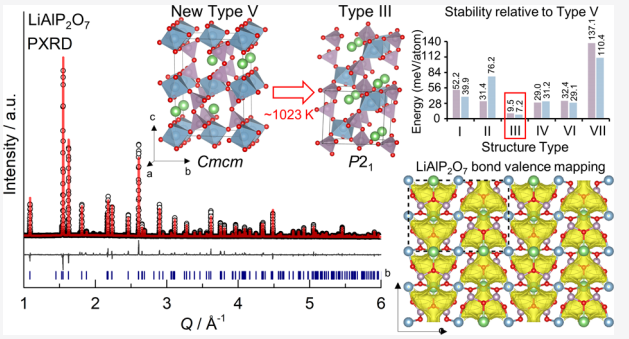

1. INTRODUCTION

All-solid-state Li batteries are a promising avenue to significantly advance Li-ion battery technology, particularly for electric vehicle applications.[1] Compared to the conventional technology, which utilizes liquid electrolytes, solid-state batteries with inorganic electrolytes are expected to offer higher pack-level power and energy densities, along with better safety performance.[1,2] These desirable features of the technology are driving a vigorous global research agenda to enable its commercial realization.[1] The materials aspects of the current research focus on finding solid electrolytes satisfying key performance metrics that include high Li-ion conductivity (≥1 mS/cm) at room temperature, stability (electrochemical, chemical, and thermal), zero/negligible electronic conductivity, good mechanical properties, and processability for large-scale industrial manufacturing.[3] Current inorganic Li solid electrolytes may be categorized into four broad classes of materials:[3] oxides (e.g., garnets[4] and LISICONs[5]), sulfides (e.g., thiophosphates[6,7] and glass ceramics[8]), halides typically mixed with a chalcogen (e.g., antiperovskites[9]), and hydrides (e.g., borohydrides[10] and closo-type complex hydrides[11]). There is great variation in the performance of these different classes of materials against the aforementioned metrics, and overall no materials have yet to be found that satisfy all of the requirements.[2,3] It is desired to develop new solid electrolyte materials by either the appropriate modification of known materials or the discovery of entirely new ones.[12]

In this study, we search for new lithium oxide materials suitable for solid electrolyte applications. In general, compared to sulfides for example, inorganic oxide solid electrolytes exhibit better chemical and electrochemical stability against Li-metal and high-voltage cathodes.[1,3,6] We selected a quinary oxide material system (compositional phase field) consisting of light elements, namely, Li, Mg, Al, P, and O, motivated by the desire for a light electrolyte. The combination of multiple cations is intended to provide the crystallographic flexibility that might support complex physicochemical properties.

A multielement phase field as studied here presents a large chemical composition space that is not feasible to sample

Received: May 11, 2021

exhaustively either through experiment or computation. Instead of sampling compositions from the entire phase field, we restricted this study to all quinary compositions with 24 O atoms in the unit cell. This leads to intermediate unit cell sizes suitable for crystal structure prediction. It should be noted that the minimum unit cell possible for quinary compositions of these elements has 6 O atoms and that this and all compositions with 8 and 12 O atoms are already included in our sample. Crystal structure prediction computations were performed within the probe structure framework,[13] where the goal is not to obtain the ground-state structure per se; instead, the aim is only to obtain a probe structure, defined as a crystal structure whose coordination environments are representative of those of the ground state at that composition. Hence, the approach reduces the computing cost by allowing termination of the structure search even before the ground state is reached. A predicted structure qualifies as a probe structure based on the nearness of its formation energy to the convex hull, but it appears that "nearness" must be determined by trial-and-error because it varies from one phase field to another. Once a probe structure is obtained, laboratory synthesis is then attempted at that composition to, hopefully, obtain the experimental ground state.

In this work, we discovered an orthorhombic polymorph of $LiAlP_2O_7$ (CCDC 2026861) while attempting to synthesize $Li_5MgAl_2P_7O_{24}$, the composition at which a probe structure had been identified. The crystal structure was solved and refined from single-crystal X-ray diffraction (XRD) data. The new orthorhombic $LiAlP_2O_7$ converts into an earlier-reported monoclinic polymorph upon heating. Li-ion conductivity was investigated by alternating-current (ac) impedance spectroscopy and solid-state NMR. Possible Li-ion-conduction pathways were mapped by bond-valence-sum (BVS) analysis. Although the pristine form of the new polymorph exhibits low Li-ion conductivity, it may be possible to devise routes for introducing suitable dopants to enhance the conductivity. Beyond its potential for solid electrolyte applications through doping, this new phase is particularly interesting because it belongs to the alkali-metal pyrophosphates, a major subclass of polyanionic compounds of technological importance in a range of applications, e.g., battery cathodes,[14] electrocatalysis,[15] phosphor host materials,[16] and nonlinear-optical materials.[17] They are characterized by high chemical and thermal stability, largely resulting from the robustness of the diphosphate anion, $[P_2O_7]^{4-}$,[14] and a rich structural diversity, often exhibiting polymorphism.[18] In the case of the $A^IM^{III}P_2O_7$ series (A = alkali metal; M = Group 13 or transition metal), rich structural diversity is reported, but the literature is not consistent in their labeling.[19−21] Adopting the notation of Hamady et al.[20] as extended by Khay et al.,[22] we further extended the structure types to include type VIII, as summarized in Table 1. Although $NaDyP_2O_7$ is reported,[23] this structure type VII is excluded from this study because a full structure solution is not available.

The cation radius ratios were calculated for the indicated prototype structures based on Shannon ionic radii.[24] Note that ionic radii employed by Vītiņš et al.[19] are the Shannon ionic radii [based on $r(O^{2-})$ = 1.26 Å recalculated for $r(O^{2-})$ = 1.32 Å].

It has been suggested that the r_A/r_M ratio is an important indicator of the structure type selection in $A^IM^{III}P_2O_7$ systems, with ratios near the lower limit (≈1.51) favoring polymorphism.[21] Furthermore, attempts have been made to develop a systematic treatment of the structural diversity including structure maps,[19] simple considerations of ionic radii,[21] and pattern recognition.[31] However, none of these approaches appears to reliably predict structure types, in contrast to related methods in other classes of materials, e.g., the Bastide diagram for ABX_4 compounds (A and B are cations, and X is an anion).[32] As is evident from Table 1, the radius ratios do not decisively discriminate among the different structure types (e.g., the values are rather close for types IV and V); indeed, Vītiņš et al.[19] reported significantly overlapping ranges for the radius ratios among the different structure types, demonstrating one limitation of the approach. In our case, the known polymorph (type III) has a radius ratio of 1.10, while that of the new (type V) is 1.26, using the less common Li coordination of 5 [Li−O bond lengths are 2.042 Å (×4) and 2.174 Å (×1)]. Five-coordinate Li has also been reported in other inorganic solids relevant to battery materials, e.g., LiB_6O_9F and $LiVPO_4F$.[33,34] If tetrahedral coordination is adopted for the Li, then the new polymorph will have the same radius ratio as its known counterpart. In either case, the radius ratio of the new polymorph is significantly smaller than the 1.77 value for KYP_2O_7 in Table 1. It is not clear that, by employing any of the current approaches for these compounds, it would have been possible to predict the existence of one of these polymorphs from knowledge of the other. Nonetheless, the relationships among these structure types are important in the search for new structural frameworks suited toward Li-ion conductivity if some structure types within the family exhibit potential for better Li-site connectivity. In such cases, attempts at chemical modifications of a composition that forms in one structure type could be made to achieve a more promising structure type.

Table 1. Structure Types of the Alkali-Metal Pyrophosphates, $A^IM^{III}P_2O_7$, Illustrating the Structural Flexibility of This Class of Materials

type	prototype	space group	Z	r_A/r_M	ref
I	$KAlP_2O_7$	$P2_1/c$ (No. 14)	4	2.97	25
II	$NaFeP_2O_7$	$P2_1/c$ (No. 14)	4	1.58	26
III	$LiFeP_2O_7$	$P2_1$ (No. 4)	2	0.91	27
IV	α-$NaTiP_2O_7$	$P2_1/c$ (No. 14)	4	1.76	28
V	KYP_2O_7	*Cmcm* (No. 63)	4	1.77	29
VI	$NaYP_2O_7$	$P2_1$ (No. 4)	2	1.13	20
VIII	$NaLaP_2O_7$	*Pnma* (No. 62)	4	1.07	30

2. EXPERIMENTAL SECTION

2.1. Probe Structure Generation and Energy Calculations. In order to search for new stable compounds from the Li−Mg−Al−P−O phase field, we first constructed the convex hull for this phase field from all ordered phases reported in the Inorganic Crystal Structure Database (ICSD). This consisted of binary, ternary, and quaternary compounds (Table S1). No quinary compounds were found from the ICSD for inclusion in the convex hull. Disordered phases were only included if it was possible to perform density functional theory (DFT) calculations on the smallest supercell containing exact integral numbers of the disordered atoms in the phase. In such a case, the lowest-energy atomic configuration obtained from a ChemDASH[35] search of up to 1000 different configurations (on the disordered sublattice) was assumed to approximate the ground state for the phase. ChemDASH is a publicly available crystal structure prediction package based on an implementation of the basin hopping method,[36] in which, for a given composition, hops between the potential energy basins are achieved through swaps in the atomic positions of selected atoms.

https://doi.org/10.1021/acs.inorgchem.1c01396
Inorg. Chem. XXXX, XXX, XXX−XXX

The convex hull is an energy surface defined by compounds that are thermodynamically stable relative to each of the other phases in the phase field from 0 K DFT calculations.[37] Such compounds are referred to as stable, and compositions with predicted energies that are close to the convex hull should be prioritized for experimental synthesis.

The DFT total energies required for the convex hull were calculated in the Vienna Ab Initio Simulation Package (VASP),[38,39] employing the projected-augmented-wave method with the Perdew−Burke−Ernzerhof (PBE) generalized gradient approximation (GGA) functional. However, where more accurate energies were required for polymorph comparisons, the meta-GGA SCAN functional,[40] known to be more accurate,[41] particularly for oxide polymorph energy rankings,[42] was used instead. A Γ-point-centered Monkhorst−Pack grid[43] was employed for k-point sampling of the Brillouin zone with a k spacing of 0.2 $Å^{-1}$, which, together with a plane-wave basis cutoff of 680 eV, ensured convergence of the total energies to better than 1 meV/atom. Each calculation was initiated from the experimental structure, and all of the lattice parameters and atomic coordinates were fully relaxed. The convex hull of the chemically stable compounds was then constructed using Pymatgen.[44]

With the convex hull constructed, 188 quinary compositions compatible with a 24-atom sublattice of close-packed O atoms were selected. This choice was initially motivated by the objective of introducing Mg and P into the α-$LiAlO_2$ structure, a common cathode coating in Li-ion batteries.[45] A probe structure was searched in ChemDASH for each of the sampled compositions as follows. A configuration was generated from a particular arrangement of the cations in the "holes" of the O sublattice. A series of low-precision DFT calculations of increasing accuracy employing the PBE GGA functional were then performed to obtain the total energy of the optimized structure for that configuration. A hop to a new configuration occurs, and the process is repeated until up to 1000 distinct configurations are visited. More accurate energies, as described above for convex hull calculations, were then finally calculated for the three best structures obtained from this process to select the probe structure.

For a geometrical estimation of potential Li-ion migration pathways and their connectivity, we employed BVS mapping,[46] an approach commonly applied to screen materials for ionic conductivity potential.[47]

2.2. Synthesis. *2.2.1. Starting Materials.* Li_2CO_3 (99.99%, dried at 523 K), Al_2O_3 (99.997%, dried at 1223 K), MgO (99.99%, dried at 1223 K), and $NH_4H_2PO_4$ (99.999%, dried at 353 K) were purchased from Sigma-Aldrich and dried at different temperatures for 20 h prior to weighing.

2.2.2. Exploratory Synthesis in the Li−Mg−Al−P−O Phase Field. Compositions in the Li−Mg−Al−P−O phase field were synthesized from stoichiometric mixtures of the starting materials using a solid-state reaction. Precursors were mixed with a mortar and pestle for 30 min with acetone added to form a paste, dried, and pressed into pellets (uniaxial press, using a 10 mm die with a pressure of 100 MPa). Pellets were transferred to a Au boat, covered with sacrificial powders (mixtures of the precursors), and heated at 873−1473 K for 40−70 h with heating and cooling rates of 1 and 5 K/min, respectively. For a selected candidate, to obtain suitable crystals for single-crystal XRD, a small batch (~0.5 g) of the precursor mixture powders was placed in a Au boat, heated at 1073 K for 4 h in air, and cooled very slowly (0.1 K/min).

2.2.3. Synthesis of Orthorhombic (Type V) $LiAlP_2O_7$ Powder. $LiAlP_2O_7$ powders were obtained by a solid-state reaction. A stoichiometric mixture of Li_2CO_3, Al_2O_3, and $NH_4H_2PO_4$ was ball-milled in ethanol with ZrO_2 balls (350 rpm for 2 h), dried, and pressed into pellets (uniaxial press, 125 MPa). Pellets were then placed in a Au boat with sacrificial powders, covered, and heated at 923−1123 K for 40 h with heating and cooling rates of 1 and 5 K/min, respectively. The sintered pellets were then ground into powders for characterization.

2.3. Diffraction. *2.3.1. Powder X-ray Diffraction (PXRD).* Laboratory PXRD data were collected on a PANalytical X'Pert Pro diffractometer with Co $K\alpha_1$ radiation (λ = 1.78901 Å) in Bragg−Brentano geometry. Patterns were recorded over the range 10−130°. Rietveld refinements were performed using *TOPAS Academic*,[48] version 5.

2.3.2. Single-Crystal XRD. A suitable crystal was selected and mounted on a Bruker D8 Venture diffractometer equipped with a Mo $K\alpha_1$ (λ = 0.71073 Å) rotating-anode source and a Bruker PHOTON 100 CMOS detector, and data were collected at room temperature. Data integration and reduction were carried out with the Bruker *SAINT*[49] software package. Face-indexed absorption correction was performed numerically using Bruker *SADABS*.[50] The structure was solved by an intrinsic phasing method using *SHELXT*,[51] implemented in *OLEX2*,[52] and refined via the *SHELXL*[53] package by least-squares minimization. The assignments of Li, Al, P, and O were determined based on the interatomic distances and relative displacement parameters. The structure was checked using the *Addsym* subroutine of *PLATON*[54] to ensure that no additional symmetry elements could be applied to the model.

2.4. ac Impedance Spectroscopy. Pellets for impedance measurements were obtained by first uniaxially pressing the resultant powders (10 mm, 100 MPa) and further pressing using a cold isostatic press (200 MPa). The resulting pellets were sintered at their optimal synthesis temperature, 923 K, for 4 h before opposite faces were coated with Au electrodes (300 nm thickness) using a Quorum Q150R sputter coater. The densities of the pellets used for impedance measurements were 65(3)% of the theoretical density. Impedance data were recorded in air with a Solartron SI 1260 analyzer with 100 mV ac voltage and a frequency range of 10^{-2}−10^{6} Hz. The obtained data were analyzed and fitted with an equivalent circuit using *ZView*[55] software version 3.3f.

2.5. Solid-State NMR. Variable-temperature ^{7}Li NMR experiments were recorded on a 4 mm HX high-temperature magic-angle-spinning probe on a 9.4 T Bruker Avance III HD spectrometer under static conditions, with the X channel tuned to ^{7}Li at $\omega_0/2\pi(^{7}\text{Li})$ = 156 MHz. Spectra were recorded with a pulse length of 1.5 μs at an radio-frequency field amplitude of $\omega_1/2\pi$ = 83 kHz and referenced to 10 M LiCl in D_2O at 0 ppm. Temperature calibrations were performed using the chemical shift thermometers $Pb(NO_3)_2$ using ^{207}Pb NMR and CuI and CuBr using ^{63}Cu NMR.[56−59] The errors associated with this method were calculated using the isotropic peak line broadening and ranged from 5 to 20 K.

3. RESULTS AND DISCUSSION

3.1. Computational/Experimental Study of the Li−Mg−Al−P−O Phase Field. From the ChemDASH study of the 188 quinary compositions, we found energies above the convex hull ranging from 34 to 244 meV/atom, Figure 1a. In particular, there are 12 compositions lying between 34 and 50 meV/atom separated from a denser band of compositions between 65 and 167 meV, which, in turn, is separated from four compositions at higher energies. Previous work[13] in our research group had suggested a high likelihood of synthesizability for compositions of up to 35 meV/atom above the hull. However, only two compositions from our sample satisfied this criterion. Because there is variation in the energy landscapes among different phase fields, we investigated what could be the most appropriate synthesizability criterion for this phase field. We considered the energies of quinary compositions that are slightly off-stoichiometric from the respective pure binary oxides (Figure 1b). We assume that the energies of such compositions do not significantly differ from those of the parent oxides because the additional metals are at very low concentrations (<0.12 on a metal-only mole fraction basis). For the selected compositions, Figure 1b shows energies above the convex hull ranging from 43 meV to an outlier at 280 meV. However, the majority of the compositions, especially the Li-rich ones, lie below 100 meV/atom, suggesting that this energy

https://doi.org/10.1021/acs.inorgchem.1c01396
Inorg. Chem. XXXX, XXX, XXX−XXX

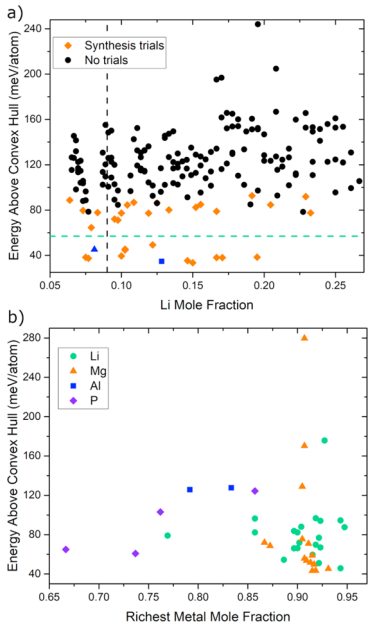

Figure 1. Energies above the convex hull. (a) Quinary compositions (expressed only as a Li mole fraction) sampled from the Li−Mg−Al−P−O phase field. The Li mole fraction basis reflects our interest in Li-rich phases. Synthesis trials were performed for most compositions below 95 meV/atom above the hull (diamond, triangle, and square symbols), and all compositions below the green dashed line are currently under investigation. $Li_5MgAl_2P_7O_{24}$, the target composition at which the new $LiAlP_2O_7$ polymorph was discovered, is indicated by the blue square. The new polymorph has also been observed in another targeted composition indicated by a blue triangle ($Li_3MgAlP_8O_{24}$). The dashed vertical line marks the Li mole fraction for $LiAlP_2O_7$. (b) Quinary compositions for synthesizability benchmarking generated by introducing small amounts of the other three metal elements into the respective binary oxides. Compositions are expressed on a metal-only mole fraction basis for the richest metal in each composition as specified in the legend.

could be a reasonable upper bound for synthesizability in this phase field. Applying this criterion, we performed synthesis trials for most compositions below 95 meV/atom (Figure 1a).

In the first stage, synthesis attempts were carried out at various temperatures (873−1473 K) with a long heat treatment to ensure reactivity of the precursors, especially refractory MgO and Al_2O_3. For the initial characterization, laboratory PXRD data were collected, and several compositions showed evidence of an unknown phase alongside reported phases available in the ICSD. Figure S1 is an example XRD pattern of the targeted composition $Li_5MgAl_2P_7O_{24}$, in which the unknown phase appears to be in a relatively high amount. Following the identification of a promising area of phase space through the appearance of an unknown phase, single-crystal growth methods were employed to isolate this new phase. Single-crystal XRD was used to determine the composition and crystal structure of the unknown phase found in sample $Li_5MgAl_2P_7O_{24}$.

3.2. Single-Crystal XRD and Crystal Structure of $LiAlP_2O_7$.

3.2.1. Diffraction. In order to identify the unknown phase in attempted sample $Li_5MgAl_2P_7O_{24}$, a single-crystal sample was prepared from the high-temperature melt. A colorless single crystal was selected and measured at room temperature. The structure of the crystal was solved and yielded a composition of $LiAlP_2O_7$. Final anisotropic atomic refinement converged to $R_1 = 0.0234$ ($wR_2 = 0.0618$) for 290 reflections with $F_o > 4\sigma(F_o)$. Crystallographic data and structural refinements for the $LiAlP_2O_7$ crystal are summarized in Table 2. The refined structural parameters and anisotropic displacement parameters of each atom are given in Tables S2 and S3, respectively. Table S4 shows selected bond distances and angles.

Table 2. Crystal Data and Structure Refinement for a Single Crystal of $LiAlP_2O_7$ Measured at 293 K

empirical formula	$LiAlP_2O_7$
fw/(g/mol)	207.86
temperature/K	293(2)
cryst syst, space group	orthorhombic, *Cmcm*
a/Å	5.1140(9)
b/Å	8.2042(13)
c/Å	11.565(3)
volume/Å^3	485.22(17)
Z	4
ρ_{calc}/(g/cm^3)	2.845
μ/mm^{-1}	1.054
F(000)	408.0
radiation	Mo Kα (λ = 0.71073)
2θ range for data collection/deg	7.046−52.884
index ranges	$-6 \le h \le 6$, $-10 \le k \le 10$, $-12 \le l \le 14$
reflns collected	2222
indep reflns	290 [R_{int} = 0.0254, R_σ = 0.0153]
completeness to θ = 25.242	99.2%
data/restraints/param	290/0/34
GOF on F^2	1.270
final *R* indexes [$I \ge 2\sigma(I)$][a]	R_1 = 0.0234, wR_2 = 0.0618
final *R* indexes (all data)[a]	R_1 = 0.0244, wR_2 = 0.0630
largest diff peak/hole/(e/Å^3)	0.30/−0.54

[a] $R_1 = \sum||F_o| - |F_c||/\sum|F_o|$ and $wR_2 = [\sum w(F_o^2 - F_c^2)^2/\sum wF_o^4]^{1/2}$ for $F_o^2 > 2\sigma(F_o^2)$.

3.2.2. Structural Description. The sample crystallizes in the orthorhombic space group *Cmcm* (No. 63) with four formula units per unit cell. Figure 2a shows the structure of $LiAlP_2O_7$ using the refined structural parameters. The Li atom occupies a 5-fold coordination site, forming a LiO_5 pseudosquare pyramid. The AlO_6 octahedra are isolated from each other, connected through corner-sharing O with pairs of PO_4 of corner-sharing tetrahedra, forming the diphosphate anion $[P_2O_7]^{4-}$. BVS calculations confirm the validity of this structural model,[60,61] with results consistent with the expected valences (Table S2).

The structure can be described as a three-dimensional framework of $^3_\infty[AlP_2O_7]^-$ constructed from the corner-sharing of alternating $[P_2O_7]^{4-}$ and AlO_6 units. The $^3_\infty[AlP_2O_7]^-$ framework affords a one-dimensional wide straight channel along the *a* axis, which is occupied by Li^+ cations, as shown in Figure 2a. Each LiO_5 unit in the channel connects with two AlO_6 octahedra via edge-sharing and three $[P_2O_7]^{4-}$ groups via corner-shared O sites, as shown in Figure 2b.

3.2.3. Comparison with Known Structures. Lithium pyrophosphates, with the general formula of $LiM^{III}P_2O_7$, present cagelike structures built from PO_4 tetrahedra and MO_6 octahedra with corner connectivity similar to those observed in orthorhombic $LiAlP_2O_7$. The voids of the one-dimensional tunnels in the framework are typically occupied by LiO_4 tetrahedra. This new polymorph is isostructural with a

https://doi.org/10.1021/acs.inorgchem.1c01396
Inorg. Chem. XXXX, XXX, XXX−XXX

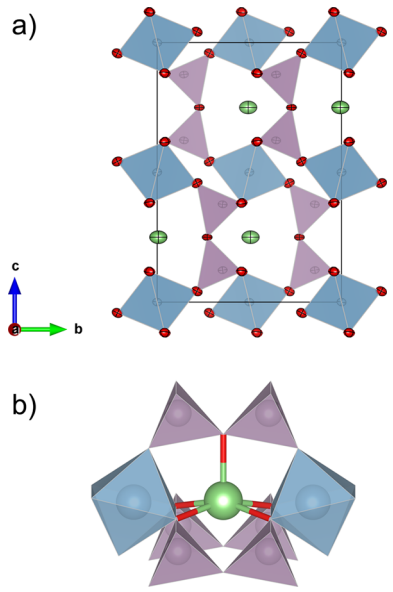

Figure 2. Crystal structure of a newly identified orthorhombic (type V) $LiAlP_2O_7$. (a) Projected views of the $LiAlP_2O_7$ structure along the *a* axis, visualizing the six-membered straight channels in the three-dimensional framework constructed from four distorted PO_4 tetrahedra (purple) and two AlO_6 octahedra (blue) sharing corners, and the Li atoms (green) are located in the voids of the channels. Atoms: Li (green), Al (blue), P (purple), and O (red). (b) Coordination environment of LiO_5 octahedra in orthorhombic $LiAlP_2O_7$ (type V).

high-temperature phase of KYP_2O_7,[29] a type V structure (Table 1), and is an isomeric polymorph of the known monoclinic $LiAlP_2O_7$ ($P2_1$).[62] The monoclinic polymorph (previously prepared by a solid-state reaction at 1073 K) was described recently[62] and is isotypic with $LiFeP_2O_7$, a type III structure (Table 1), crystallizing in the monoclinic space group $P2_1$ with refined lattice parameters: a = 4.81 Å, b = 8.09 Å, c = 6.96 Å, and β = 109.22°. The monoclinic polymorph can be described in terms of AlO_6, P_2O_7, and LiO_4 units. Because the experimental atomic coordinates were not reported for monoclinic $LiAlP_2O_7$, our discussion of the bond lengths and angles refers to values extracted from a DFT-optimized structure. The LiO_4 tetrahedra in the monoclinic polymorph are highly distorted, with Li−O distances ranging from 1.904 and 2.066 Å and O−Li−O angles in the range of 80.452−170.536°. Different from the eclipsed conformation in the orthorhombic polymorph, the pyrophosphate group of the monoclinic polymorph is slightly staggered with a dihedral angle of 9.76°. The smaller P−O−P angle for the known monoclinic polymorph indicates a bending about the bridging O atom, slightly compressing the diphosphate ion, consistent with the ∼2% higher density of this polymorph. The distance between the P atoms of the P−O−P unit is 2.9322 Å for the known polymorph, while that for the new structure is longer at 2.976(1) Å. For simplicity of notation, we henceforth adopt the structure-type notation of Table 1, i.e., type III (known monoclinic polymorph) and type V (new orthorhombic polymorph).

Related isostructural compounds of type III $LiAlP_2O_7$,[62] such as $LiCrP_2O_7$,[63,64] $LiFeP_2O_7$,[19,27] $LiScP_2O_7$,[19] and $LiGaP_2O_7$,[65] can be described as three-dimensional cage structures constructed from the corner-sharing of alternating P_2O_7 and MO_6 (M = Cr, Fe, Sc, and Ga) units, and the voids in the framework are occupied by Li cations. All of these type III structures have wide straight tunnels, which provide possible pathways for Li-ion diffusion. In addition, the type III polymorph, as well as other lithium pyrophosphates in the $LiM^{III}P_2O_7$ family, presents shorter Li−Li distances compared to the type V $LiAlP_2O_7$ reported in this work (Figure 3 and Table 3).

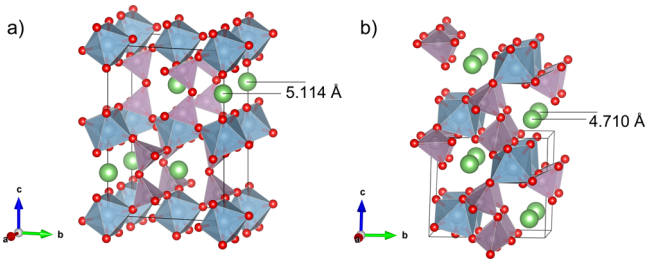

Figure 3. Comparison of the crystal structures of (a) orthorhombic (*Cmcm*) $LiAlP_2O_7$ and (b) monoclinic ($P2_1$) $LiAlP_2O_7$. Labels show the Li−Li distances between highlighted Li positions.

3.3. Synthesis of Phase-Pure Type V $LiAlP_2O_7$ and Phase Stability.

3.3.1. Synthesis, Diffraction, and Structure Refinements. Because type V $LiAlP_2O_7$ was identified as a new polymorph through the method described above, attempted powder synthesis and purification were carried out following single-crystal growth. Multiple firings were performed in the range of 923−1123 K, and $LiAlP_2O_7$ was successfully synthesized via a solid-state reaction route using a heat treatment at 973 K. Samples prepared at this temperature were found to be single phase by laboratory PXRD (Figure 4). All reflections were indexed using the orthorhombic space group *Cmcm*, a = 5.112096(19) Å, b = 8.21605(3) Å, and c = 11.60739(5) Å. The crystal structure of powder samples was confirmed through Rietveld refinement using the single-crystal model as a starting point. All refinement parameters, including goodness-of-fit χ^2 = 6.64 and R_{wp} factor = 10.09%, are acceptable. These results indicate that a single-phase powder of type V $LiAlP_2O_7$ can be reproducibly synthesized using a heat treatment at 973 K for 40 h.

3.3.2. Reaction Conditions and Phase Transition. The results of attempted syntheses at different temperatures of $LiAlP_2O_7$ are summarized in Table 4. The PXRD patterns of these samples are shown in Figure S2. The new type V $LiAlP_2O_7$ could only be synthesized phase-pure at ∼973 K. Type III $LiAlP_2O_7$ is the reaction product at 1023 K and was previously reported as an isomorphic compound of $LiFeP_2O_7$ by Taher et al.[62] However, their samples prepared at 1073 K were not phase-pure. Here, by sintering a stoichiometric mixture of precursors at 1023 K for 40 h, the reported[62] type III $LiAlP_2O_7$ was successfully synthesized as a single phase. The PXRD data measured from this sample were indexed to a monoclinic unit cell with dimensions a = 4.71614(2) Å, b = 7.80512(3) Å, c = 6.81279(2) Å, and β = 108.4549(4)° (Tables S5 and S6). Experimental and calculated XRD patterns are shown in Figure S3.

As $LiAlP_2O_7$ is at least dimorphic, in order to explore any phase transition, a sample sintered at 973 K was reheated at a higher temperature, 1023 K, for 4 h. Figure 5 gives a comparison of the XRD patterns before and after reheating, presenting evidence for a partial phase transformation of the

https://doi.org/10.1021/acs.inorgchem.1c01396
Inorg. Chem. XXXX, XXX, XXX−XXX

Table 3. Li−Li Distances in Related Lithium Pyrophosphates along the Li Channels

compound	structure	space group	Li−Li distance (Å)	ref
$LiAlP_2O_7$	orthorhombic	*Cmcm* (No. 63)	5.114	this work
$LiAlP_2O_7$	monoclinic	$P2_1$ (No. 4)	4.710	62
$LiFeP_2O_7$	monoclinic	$P2_1$ (No. 4)	4.823	19, 27
$LiCrP_2O_7$	monoclinic	$P2_1$ (No. 4)	4.787	63, 64
$Li_4P_2O_7$	monoclinic	$P2_1/c$ (No. 14)	2.998−3.214	66−69
$Li_5CsMn(P_2O_7)_2$	orthorhombic	*Pbcn* (No. 60)	2.490−3.277	70

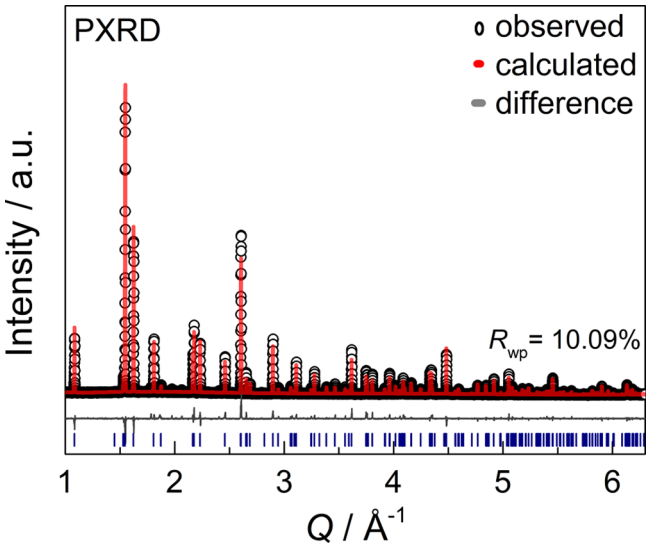

Figure 4. Experimental (black circles), calculated (red line), and difference (gray line) profiles illustrating the quality of the Rietveld fit to PXRD (Co Kα_1 radiation) of the as-synthesized orthorhombic type V polymorph of $LiAlP_2O_7$.

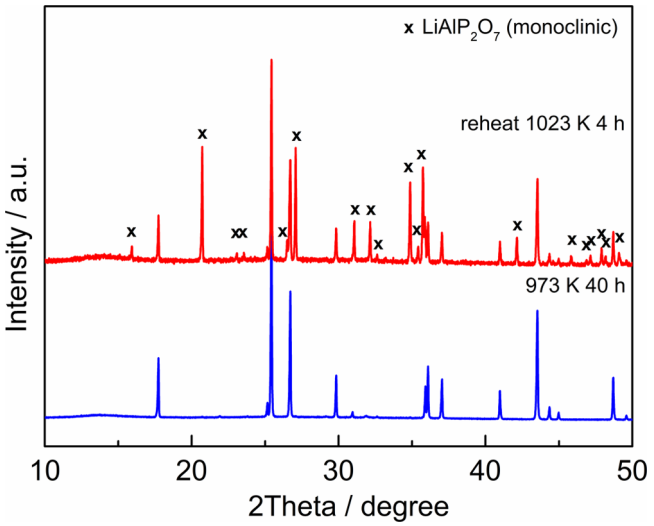

Figure 5. XRD patterns, Co Kα_1 radiation, of the as-synthesized orthorhombic $LiAlP_2O_7$ and the same powder after reheating to 1023 K for 4 h. Crosses indicate reflections from the monoclinic type III polymorph of $LiAlP_2O_7$.

Table 4. Phases Present in Samples Heated at Different Temperatures as Determined by PXRD

no.	temperature (K)	phases present
1	923	type V $LiAlP_2O_7$, $LiPO_3$, $Al(PO_3)_3$
2	973	type V $LiAlP_2O_7$
3	1023	type III $LiAlP_2O_7$
4	1073	$AlPO_4$, $LiPO_3$
5	1123	$AlPO_4$, $LiPO_3$

type V low-temperature form into the type III high-temperature form occurring at temperatures above ∼1023 K.

Our DFT results show that the type V polymorph is lower in energy at 7.2 meV/atom (PBE functional) and 9.5 meV/atom (SCAN) compared to the type III polymorph. For quaternary systems, the median total energy of polymorphs above the "ground-state polymorph" is 3.4 meV/atom,[71] suggesting that the type V polymorph is substantially more stable than the type III phase at 0 K. This is consistent with the type V polymorph being accessible experimentally at lower temperature. Two aspects of the phase transition between the polymorphs can be noted. First, the qualitative DFT relative stability of the polymorphs is considered reliable because comparisons between the PBE and SCAN functionals show the latter giving results closer to experiment for many oxides,[72] even in such challenging cases as the anatase/rutile phase transition of TiO_2.[73] Although we found no DFT reports of polymorph relative stabilities for the more closely related $A^IM^{III}P_2O_7$ family of compounds (M = Al, Ga, and In) for comparison, examples have been reported for transition-metal pyrophosphates and for phosphates in general. Apart from the added complexity of d orbitals in transition-metal-based pyrophosphates, polymorph relative energies qualitatively alongside experiment have been reported for these compounds, e.g., $Na_2FeP_2O_7$[74] and $Na_2CoP_2O_7$.[75] Similar findings are also reported for phosphates (containing transition metals) in general, e.g., $VOPO_4$,[76] $BaM_2(PO_4)_2$ (M = Mn, Fe, and Co),[77] and $NaNiPO_4$.[78] Except for highly correlated oxides (e.g., CoO[79] and MnO[80]) requiring higher-level theories,[81] DFT employing semilocal or hybrid functionals is commonly successful in obtaining qualitatively correct ordering of polymorph energies in simple oxides, e.g., MgO,[82] Al_2O_3,[83] and ZnO.[84]

Second, while $P2_1$ is a subgroup of *Cmcm*, they are not connected by a single irreducible representation (irrep) order parameter (i.e., it is not a simple Landau-type phase transition);[84] instead, the two structures have a complex maximal subgroup structure, suggesting a first-order transition. The phase transition could involve multiple irrep order parameters, but it is more likely to be completely reconstructive. The exact path for phase transitions of this type can be quite complex and counterintuitive. For example, Bianchini et al.[85] recently reported the somewhat counterintuitive observation of a DFT ground-state polymorph forming at a higher temperature than those of the polymorphs predicted to be metastable. This was rationalized from direct in situ observation of the progress of the solid-state reaction, where the interplay between the exact experimental thermody-

https://doi.org/10.1021/acs.inorgchem.1c01396
Inorg. Chem. XXXX, XXX, XXX−XXX

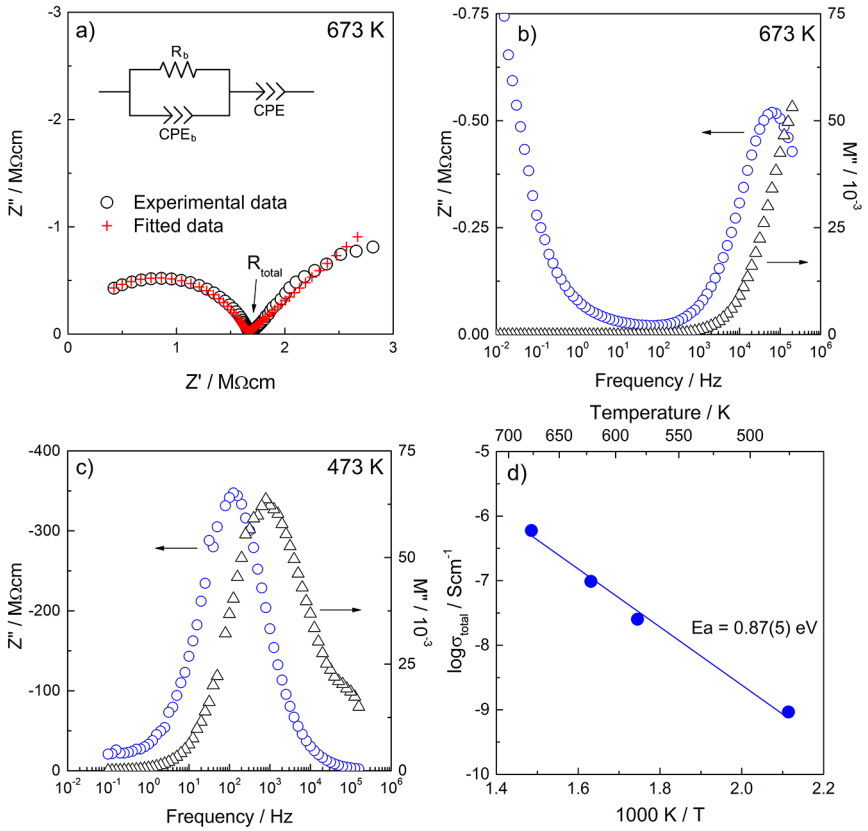

Figure 6. Impedance data for type V $LiAlP_2O_7$ sintered at 973 K and measured in air. (a) Impedance plots at 673 K. (b and c) Z''/M'' spectroscopic plots at 673 and 473 K. (d) Arrhenius plots of the total conductivity data. The equivalent circuit used to model the data is inset in part a.

namics and kinetics selected a multiple-step pathway involving the metastable polymorphs as intermediate phases.

3.4. Li Conductivity. *3.4.1. ac Impedance Spectroscopy.* The electrical properties of type V $LiAlP_2O_7$ were determined by ac impedance spectroscopy on a sintered pellet with ~65% relative density. Typical impedance data sets recorded at 673 and 473 K are shown in Figure 6.

The impedance complex plane plots (Figure 6a) show a single arc at high frequencies and an inclined spike with some curvature at low frequencies. The high-frequency arc is attributed to the sample bulk because the corresponding Z''/M'' spectra (Figure 6b,c) show single and almost overlapping peaks, which is clearer at lower temperature. The low-frequency spike is attributed to the electrode double-layer phenomenon. In general, the material is electrically homogeneous, and the impedance response is mainly dominated by the sample bulk. Thus, the high-frequency impedance data could be represented by the parallel R-CPE element shown in Figure 6a (inset), in which CPE is a constant phase element responsible for the dispersion seen in both the C' (Figure S4) and Z''/M'' data. The conductivity data were extracted from the low-frequency intercepts in the Z^* plot and plotted in an Arrhenius format in Figure 6d. Almost linear behavior was observed in the temperature range 473−673 K. Type V $LiAlP_2O_7$ is, therefore, a modest Li-ion conductor with a conductivity of 6×10^{-7} S/cm at 673 K and an activation energy of 0.87(5) eV.

3.4.2. Solid-State NMR. The temperature dependence of the static ^{7}Li NMR spectra of type V $LiAlP_2O_7$ over the 295−583 K temperature range is shown in Figure 7 and shows a

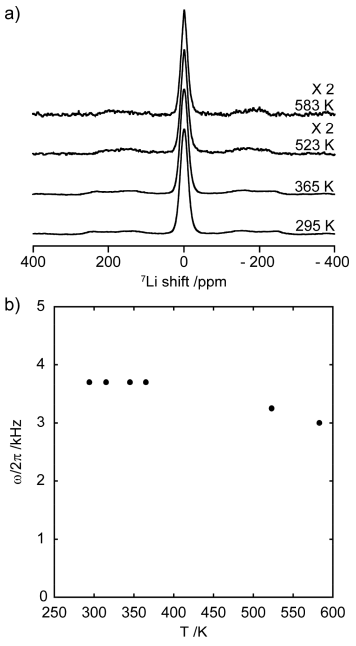

Figure 7. (a) Static ^{7}Li NMR spectra as a function of the temperature for type V $LiAlP_2O_7$. Spectra at temperatures of 523 and 583 K were recorded with half the number of transients and have been scaled up by a factor of 2 for comparison. (b) Temperature dependence of the ^{7}Li NMR central transition line width.

resonance at 0 ppm corresponding to the ^{7}Li central transition (^{7}Li is spin $^3/_2$) as well as the corresponding satellite

https://doi.org/10.1021/acs.inorgchem.1c01396
Inorg. Chem. XXXX, XXX, XXX−XXX

Table 5. Structural Symmetry, Unit Cell Volume, Li−Li Distances, and Ionic Conductivities of $A^IM^{III}P_2O_7$-Type Pyrophosphates and Selected Lithium Phosphates

compound	structure	space group	V/Z (Å^3)	σ_{total} at 573 K[a] (S/cm)	minimum Li−Li distance (Å)	E_a (eV)	ref
$LiAlP_2O_7$	orthorhombic	*Cmcm* (No. 63)	121.3	5.0×10^{-8}	5.114	0.87	this work
$LiAlP_2O_7$	monoclinic	$P2_1$ (No. 4)	135.4	*8.1 × 10^{-6}*	4.710	0.84	62
$LiScP_2O_7$	monoclinic	$P2_1$ (No. 4)	137.1	4.1×10^{-7}	4.940	1.06	19
$LiFeP_2O_7$	monoclinic	$P2_1$ (No. 4)	143.9	8.3×10^{-7}	4.823	1.23	19, 27
$Li_4P_2O_7$	monoclinic	$P2_1/c$ (No. 14)	142.5	*3.2 × 10^{-6}*	2.998	0.99	66−69
$Li_{12}Zn_4(P_2O_7)_5$	monoclinic	$P2_1/c$ (No. 14)	141.6	*3.9 × 10^{-4}*	2.607	0.79	68, 69, 86
$LiZr_2(PO_4)_3$	rhombohedral	$R\bar{3}c$ (No. 167)	250.6	1.2×10^{-2}	1.457	0.42	87, 88
$LiGd(PO_3)_4$	monoclinic	$C2/c$ (No. 15)	226.1	*9.5 × 10^{-8}*	5.622	1.76	89
$LiMg_3(PO_4)P_2O_7$	orthorhombic	*Pnma* (No. 62)	199.1	*2.1 × 10^{-7}*	6.87	1.17	90
$Li_5CsMn(P_2O_7)_2$	orthorhombic	*Pbcn* (No. 60)	315.8	1.3×10^{-5}	2.490	0.42	70

[a]Values in italic type are interpolated from Arrhenius plots.

transitions spanning hundreds of parts per million. In static solid-state ^{7}Li NMR spectra and in the absence of Li-ion mobility, this central transition is broadened by the strong homonuclear ^{7}Li−^{7}Li dipolar coupling interactions (so-called rigid lattice regime). Type V $LiAlP_2O_7$ remains in this regime until roughly 500 K and has a line width of approximately 3.7 kHz. As the temperature is increased to 523 and 583 K, a small decrease of the NMR line width of only 0.7 kHz was observed, indicating limited averaging of the ^{7}Li−^{7}Li dipolar interactions due to a slight increase in the Li-ion motion. Higher temperatures were not accessed because of restrictions on the temperature range of the available NMR probe hardware. This absence of significant NMR line narrowing suggests that Li-ion mobility in type V $LiAlP_2O_7$ is minimal in the measured temperature range and consistent with the large Li−Li distance (Table 5) and conductivity measured from ac impedance.

3.4.3. Conduction Mechanism of Pyrophosphates. Compared to other reported pyrophosphates (Table 5), type V $LiAlP_2O_7$ exhibits a lower but comparable ionic conductivity. A clear correlation between the measured ionic conductivity and minimum Li−Li distance emerges from this comparison, as shown in Figure 8. This probably indicates that all of these pyrophosphates share a similar primary Li-conduction mechanism, suggested to be associated with the cage frameworks common to all of these structures.[19,62,90] As shown in Figure 9, it is likely that Li-ion transport in pyrophosphates occurs primarily by a hopping mechanism of Li ions along these channels. However, despite their generic framework structure, the different structure types of these pyrophosphates exhibit varying structural characteristics, potentially leading to different topologies for the Li sublattices. Some of these topologies could be more favorable to long-range Li-ion migration than others. Accordingly, we examine seven of the structure types in Table 1 (Figure 9) by BVS mapping to assess the prospect for favorable Li-ion conductivity of $LiAlP_2O_7$ forming in each of the structure types.

The BVS maps, calculated for crystal structures optimized in DFT, are plotted in Figure 10a−g. Note that, except for the type III and V polymorphs, the rest of the structures are hypothetical for the composition $LiAlP_2O_7$. We have also included their energies relative to the type V polymorph, the most stable form at low temperature, to provide a rough estimate of the minimum energy barriers for structural transition to the higher-energy forms. The BVS maps show that only types I and III exhibit three-dimensional isosurface connectivity (Figure 10a,c), although the *c*-direction connectivity for the latter is significantly limited. Type II has no connected pathways (Figure 10b), while types IV, V, and VIII all lack *c*-direction connectivity (Figure 10d,e,g). For types I−III, V, and VIII, the Li−Li distances for long-range connectivity are ≥4 Å, suggesting alongside the correlation between the Li−Li distance and conductivity shown in Figure 8 that an effective strategy to enhance Li conduction will likely require reduction of these Li−Li distances, i.e., introducing interstitial Li atoms. This approach could be particularly effective for the type I case because it offers a more open structure (Figure 10a) provided the energetics are favorable. Types IV and VI are intriguing; while introducing Li vacancies into the zigzag chains in the *b* direction (Figure 9d,f) might enhance Li conduction, the SCAN energies for both structure types are too close to that for type II, which might make structure-type selectivity challenging. Nonetheless, if innovative doping schemes could be devised to realize type IV and VI structures for $LiAlP_2O_7$,

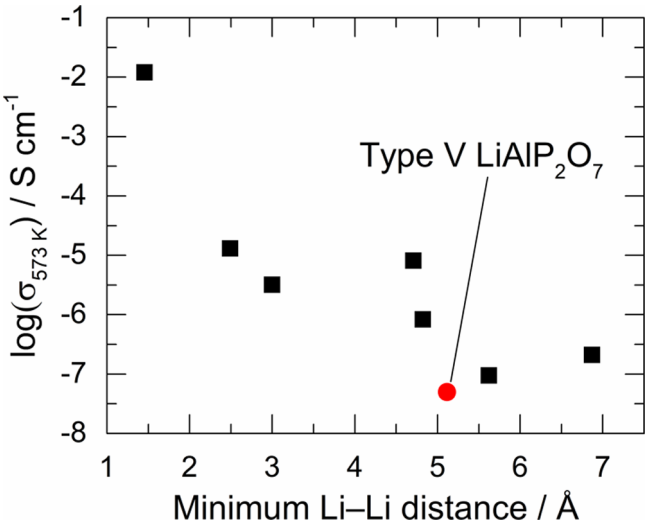

Figure 8. Comparison of Li-ion conductivity at 573 K against the minimum Li−Li distance for the $A^IM^{III}P_2O_7$-type pyrophosphates and selected lithium phosphates (black squares) given in Table 5.[27,62,67,70,87−90] Type V $LiAlP_2O_7$ reported in this work is highlighted (red circle). Reproduced with permission from ref 27. Copyright 2016 Elsevier. Reproduced with permission from ref 62. Copyright 2016 Elsevier. Reproduced with permission from ref 67. Copyright 2014 Elsevier. Reproduced with permission from ref 70. Copyright 2003 Royal Society of Chemistry. Reproduced with permission from ref 87. Copyright 2003 American Chemical Society. Reproduced with permission from ref 89. Copyright 2006 Elsevier. Reproduced with permission from ref 90. Copyright 2015 Elsevier.

https://doi.org/10.1021/acs.inorgchem.1c01396
Inorg. Chem. XXXX, XXX, XXX−XXX

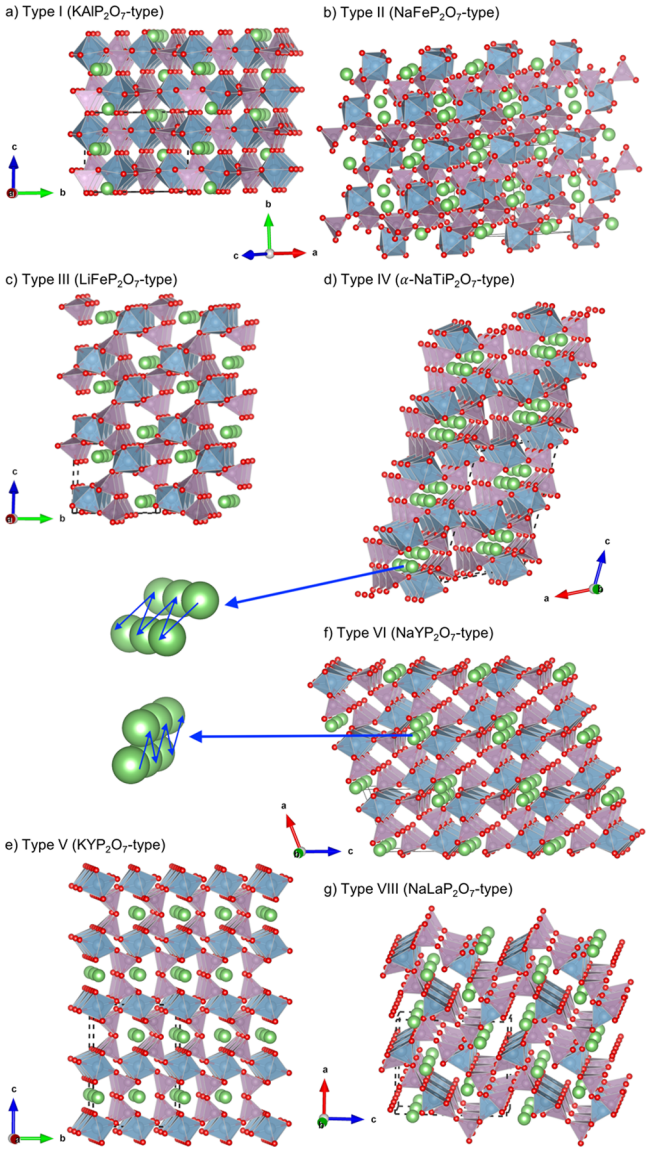

Figure 9. Structure types from Table 1 depicting the Li channels that result from cage frameworks formed from different arrangements of corner-sharing PO_4 tetrahedra (purple) and AlO_6 octahedra (blue). Types III (c) and V (e) are the known and new polymorphs of $LiAlP_2O_7$, respectively, while the rest are hypothetical structure types for $LiAlP_2O_7$. Both types IV and VI have zigzag Li chains in the *b* direction as shown.

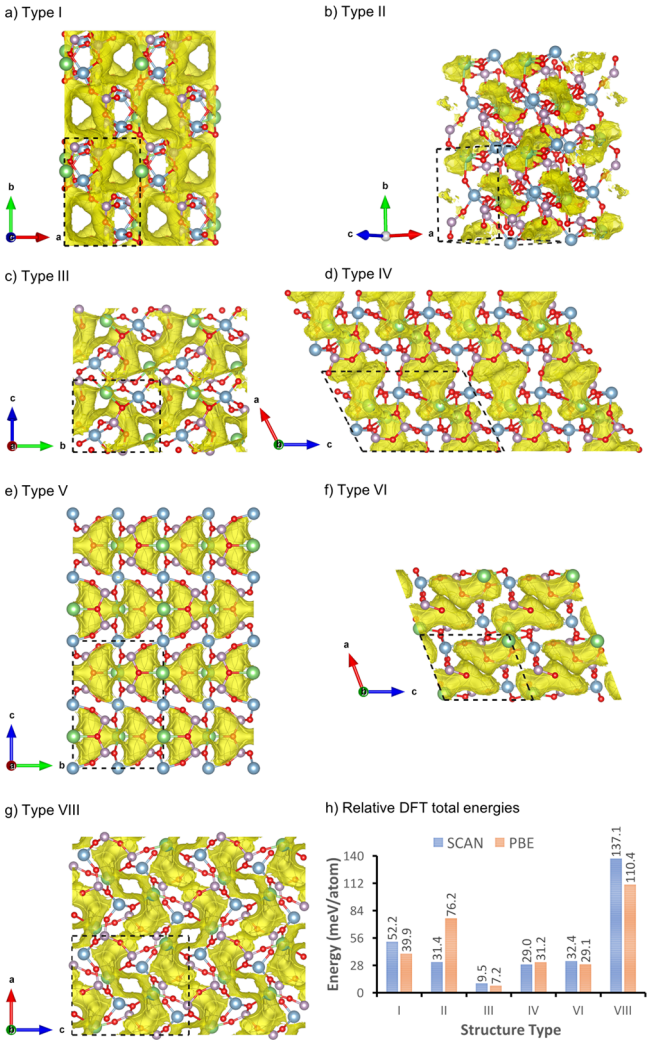

Figure 10. Isosurfaces (yellow) at a Li BVS of 1.0 valence unit to highlight potential pathways for Li-ion conduction in the different structure types (a–g) and DFT total energies relative to the new polymorph (h). Type I: three-dimensional connectivity of the isosurfaces, but the Li–Li distances (>4 Å) are too long. Type II: no connected pathways; the Li sublattice consists of Li "dimers" (Li–Li distance of 2.8 Å) that are >5.2 Å apart. Type III: weak *c*-direction connectivity; Li–Li distances >4 Å are too long. Type IV: no *c*-direction connectivity; the Li–Li distance in the *b*-direction zigzag chains is 3.1 Å and could be favorable for Li-ion conductivity; *a*-direction isosurfaces connect Li sites ~7 Å apart. Type V: no *c*-direction connectivity; Li–Li distances >4 Å are too long. Type VI: no *a*-direction connectivity; *b*-direction zigzag Li chains (Li–Li distance ~2.8 Å) could be favorable to Li migration; isosurfaces in the [101] direction connect Li sites ~8.3 Å apart. Type VIII: no *c*-direction connectivity; Li–Li distances ≥4 Å are too long. The SCAN (PBE) energies vary from 9.5 meV (7.2 meV) for type III to 137.1 meV (110.4 meV) for type VIII relative to the new polymorph. Type V is the most stable structure type for the composition $LiAlP_2O_7$ at low temperature. The SCAN energies for types II, IV, and VI are remarkably close to each other. At almost 2.5× larger than the SCAN value, the PBE energy for type II presents an apparent anomaly among the energy results, but the reason for this is unclear. Dashed lines indicate the unit cell, and atom colors are green, blue, purple, and red for Li, Al, P, and O, respectively.

they would likely yield the best Li conductivity among all seven structure types. A caveat to this discussion of the energetics of the structure types is that, because the actual energy barriers for structural transition are unknown, only a naive consideration of the energetics is possible. Furthermore, dopants could be introduced to the type III polymorph instead of the type V polymorh, thus improving the overall energetics according to this naive analysis.

3.4.4. Comparison with Known Phosphates. Although the above $A^IM^{III}P_2O_7$-type pyrophosphates have a framework with wide tunnels for Li^+-ion transportation, the ionic conductivities in these materials are low, 10^{-6}–10^{-8} S/cm at 573 K (Table 5). Appreciable Li-ion conductivity is always found in open-framework or layered materials containing mobile Li cations. In particular, many phosphates are good ionic conductors, notably NASICON,[91−93] which is widely known to be a fast ion conductor. Different from NASICON-related structures, it is clear that the framework structures of pyrophosphates are, in general, not suited to fast ion conductivity.

https://doi.org/10.1021/acs.inorgchem.1c01396
Inorg. Chem. XXXX, XXX, XXX−XXX

The most likely reasons for the low conductivity observed in both type III and V $LiAlP_2O_7$ polymorphs despite their wide one-dimensional Li channels include the following: (i) a lack of disordered or partially ordered sites and the absence of Li defects (vacancies and interstitials) in the structure, whereas in comparison with a structure like NASICON, both Li site disordering and partial occupancy of a large number of possible sites play a key role in the high mobility;[92−94] (ii) Li−Li distances that are too long to ensure continuous transport pathways between Li sites available for Li-ion hopping (Table 5). In contrast, shorter Li−Li distances are observed in compounds such as $Li_{12}Zn_4(P_2O_7)_5$ and $Li_5CsMn(P_2O_7)_2$, which show higher conductivities (1−3 orders of magnitude) than other pyrophosphates.[19,27,62,66−70,86−90] Accordingly and supported by calculation, we have suggested the introduction of Li vacancies in the two structure types with comparatively short Li−Li distances.

4. CONCLUSIONS

We reported a new polymorph of $LiAlP_2O_7$, guided by a workflow incorporating crystal structure prediction. The structure was indexed to an orthorhombic unit cell with parameters a = 5.1140(9) Å, b = 8.2042(13) Å, c = 11.565(3) Å, and V = 485.22(17) Å^3. Static solid-state ^{7}Li NMR spectroscopy on powdered samples revealed minimum Li-ion mobility up to 583 K. Impedance measurements on sintered pellets showed a homogeneous bulk response with no significant grain boundary impedance and a poor Li-ion conductivity of 6×10^{-7} S/cm at 673 K, likely not competitive as an electrolyte for all solid-state batteries. However, by examining the structure types observed for the $A^IM^{III}P_2O_7$ family of compounds, we have suggested potential avenues for enhancing the Li-ion conductivity within this broad materials family. Finally, future work could also focus on an in-depth study of the structural phase transition between the new and known polymorphs to gain insight into the mechanisms involved.

■ ASSOCIATED CONTENT

Supporting Information

The Supporting Information is available free of charge at https://pubs.acs.org/doi/10.1021/acs.inorgchem.1c01396.

Isolation of phase-pure orthorhombic $LiAlP_2O_7$ through synthesis at different temperatures, structural information for orthorhombic $LiAlP_2O_7$, Rietveld refinement and structural details of the known monoclinic phase of $LiAlP_2O_7$ from PXRD data, and typical impedance data set at 673 K of phase-pure orthorhombic $LiAlP_2O_7$ (PDF)

Accession Codes

CCDC 2026861 contains the supplementary crystallographic data for this paper. These data can be obtained free of charge via www.ccdc.cam.ac.uk/data_request/cif, or by emailing data_request@ccdc.cam.ac.uk, or by contacting The Cambridge Crystallographic Data Centre, 12 Union Road, Cambridge CB2 1EZ, UK; fax: +44 1223 336033.

■ AUTHOR INFORMATION

Corresponding Author

Matthew J. Rosseinsky − *Department of Chemistry, University of Liverpool, Liverpool L69 7ZD, U.K.;* orcid.org/0000-0002-1910-2483; Email: M.J.Rosseinsky@liverpool.ac.uk

Authors

Elvis Shoko − *Department of Chemistry, University of Liverpool, Liverpool L69 7ZD, U.K.*

Yun Dang − *Department of Chemistry, University of Liverpool, Liverpool L69 7ZD, U.K.;* orcid.org/0000-0002-0140-0140

Guopeng Han − *Department of Chemistry, University of Liverpool, Liverpool L69 7ZD, U.K.*

Benjamin B. Duff − *Department of Chemistry, University of Liverpool, Liverpool L69 7ZD, U.K.; Stephenson Institute for Renewable Energy, University of Liverpool, Liverpool L69 7ZF, U.K.;* orcid.org/0000-0002-7398-5002

Matthew S. Dyer − *Department of Chemistry, University of Liverpool, Liverpool L69 7ZD, U.K.*

Luke M. Daniels − *Department of Chemistry, University of Liverpool, Liverpool L69 7ZD, U.K.;* orcid.org/0000-0002-7077-6125

Ruiyong Chen − *Department of Chemistry, University of Liverpool, Liverpool L69 7ZD, U.K.;* orcid.org/0000-0002-5340-248X

Frédéric Blanc − *Department of Chemistry, University of Liverpool, Liverpool L69 7ZD, U.K.; Stephenson Institute for Renewable Energy, University of Liverpool, Liverpool L69 7ZF, U.K.;* orcid.org/0000-0001-9171-1454

John B. Claridge − *Department of Chemistry, University of Liverpool, Liverpool L69 7ZD, U.K.*

Complete contact information is available at: https://pubs.acs.org/10.1021/acs.inorgchem.1c01396

Author Contributions

†These authors contributed equally.

Notes

The authors declare no competing financial interest.

Underlying data are available at http://datacat.liverpool.ac.uk/id/eprint/1153.

■ ACKNOWLEDGMENTS

We are grateful to the ISCF Faraday Challenge project "SOLBAT—The Solid-State (Li or Na) Metal-Anode Battery" (Grant FIRG007) including partial support of a studentship to B.B.D., also supported by the University of Liverpool. The U.K. Materials and Molecular Modelling Hub is thanked for computational resources, which is partially funded by the EPSRC (Grant EP/P020194/1). E.S. thanks Dr. P. Sharp for technical assistance with ChemDASH. We thank the EPSRC for funding G.H. under Grant EP/N004884. M.J.R. thanks the Royal Society for the award of a Research Professorship.

■ REFERENCES

(1) Zheng, F.; Kotobuki, M.; Song, S.; Lai, M. O.; Lu, L. Review on Solid State Electrolytes for All-Solid-State Lithium-Ion Batteries. *J. Power Sources* **2018**, *389*, 198−213.

(2) Randau, S.; Weber, D. A.; Kötz, O.; Koerver, R.; Braun, P.; Weber, A.; Ivers-Tiffée, E.; Adermann, T.; Kulisch, J.; Zeier, W. G.; Richter, F. H.; Janek, J. Benchmarking the Performance of All-Solid-State Lithium Batteries. *Nat. Energy* **2020**, *5*, 259−270.

(3) Manthiram, A. An Outlook on Lithium Ion Battery Technology. *ACS Cent. Sci.* **2017**, *3*, 1063−1069.

(4) Murugan, R.; Thangadurai, V.; Weppner, W. Fast Lithium Ion Conduction in Garnet-Type $Li_7La_3Zr_2O_{12}$. *Angew. Chem., Int. Ed.* **2007**, *46*, 7778−7781.
(5) Deng, Y.; Eames, C.; Fleutot, B.; David, E.; Chotard, J.; Suard, E.; Masquelier, C.; Islam, M. S. Enhancing the Lithium Ion Conductivity in Lithium Superionic Conductor (LISICON) Solid Electrolytes through a Mixed Polyanion Effect. *ACS Appl. Mater. Interfaces* **2017**, *9*, 7050−7058.
(6) Kato, Y.; Hori, S.; Saito, T.; Suzuki, K.; Hirayama, M.; Mitsui, A.; Yonemura, M.; Iba, H.; Kanno, R. High-Power All-Solid-State Batteries using Sulfide superionic Conductors. *Nat. Energy* **2016**, *1*, 16030.
(7) Kraft, M. A.; Ohno, S.; Zinkevich, T.; Koerver, R.; Culver, S. P.; Fuchs, T.; Senyshyn, A.; Indris, S.; Morgan, B. J.; Zeier, W. G. Inducing High Ionic Conductivity in the Lithium Superionic Argyrodites $Li_{6+x}P_{1-x}Ge_xS_5I$ for All-Solid-State Batteries. *J. Am. Chem. Soc.* **2018**, *140*, 16330−16339.
(8) Mizuno, F.; Hayashi, A.; Tadanaga, K.; Tatsumisago, M. High Lithium Ion Conducting Glass-Ceramics in the System Li_2S-P_2S_5. *Solid State Ionics* **2006**, *177*, 2721−2725.
(9) Lü, X.; Wu, G.; Howard, J. W.; Chen, A.; Zhao, Y.; Daemen, L. L.; Jia, Q. Li-Rich Anti-Perovskite Li_3OCl Films with Enhanced Ionic Conductivity. *Chem. Commun.* **2014**, *50*, 11520−11522.
(10) Matsuo, M.; Nakamori, Y.; Orimo, S.; Maekawa, H.; Takamura, H. Lithium Superionic Conduction in Lithium Borohydride Accompanied by Structural Transition. *Appl. Phys. Lett.* **2007**, *91*, 224103.
(11) Kim, S.; Oguchi, H.; Toyama, N.; Sato, T.; Takagi, S.; Otomo, T.; Arunkumar, D.; Kuwata, N.; Kawamura, J.; Orimo, S. A Complex Hydride Lithium Superionic Conductor for High-Energy-Density All-Solid-State Lithium Metal Batteries. *Nat. Commun.* **2019**, *10*, 1081.
(12) Ohno, S.; Banik, A.; Dewald, G. F.; Kraft, M. A.; Krauskopf, T.; Minafra, N.; Till, P.; Weiss, M.; Zeier, W. G. Materials Design of Ionic Conductors for Solid State Batteries. *Prog. Energy* **2020**, *2*, 022001.
(13) Collins, C.; Dyer, M. S.; Pitcher, M. J.; Whitehead, G. F. S.; Zanella, M.; Mandal, P.; Claridge, J. B.; Darling, G. R.; Rosseinsky, M. J. Accelerated Discovery of Two Crystal Structure Types in a Complex Inorganic Phase Field. *Nature* **2017**, *546*, 280−284.
(14) Barpanda, P.; Nishimura, S. I.; Yamada, A. High-Voltage Pyrophosphate Cathodes. *Adv. Energy Mater.* **2012**, *2*, 841−859.
(15) Song, H. J.; Yoon, H.; Ju, B.; Lee, D. Y.; Kim, D. W. Electrocatalytic Selective Oxygen Evolution of Carbon-Coated $Na_2Co_{1-x}Fe_xP_2O_7$ Nanoparticles for Alkaline Seawater Electrolysis. *ACS Catal.* **2020**, *10*, 702−709.
(16) Xu, M.; Ding, Y.; Luo, W.; Wang, L.; Li, S.; Liu, Y. Synthesis, Luminescence Properties and Energy Transfer Behaviour of Colour-Tunable $KAlP_2O_7$: Tb^{3+}, Eu^{3+} Phosphors. *Opt. Laser Technol.* **2020**, *121*, 105829.
(17) Zhao, S.; Yang, X.; Yang, Y.; Kuang, X.; Lu, F.; Shan, P.; Sun, Z.; Lin, Z.; Hong, M.; Luo, J. Non-Centrosymmetric $RbNaMgP_2O_7$ with Unprecedented Thermo-Induced Enhancement of Second Harmonic Generation. *J. Am. Chem. Soc.* **2018**, *140*, 1592−1595.
(18) Durif, A. *Crystal Chemistry of Condensed Phosphates*; Springer USA, 1995.
(19) Vītiņš, Ģ.; Kaņepe, Z.; Vītiņš, A.; Ronis, J.; Dindūne, A.; Lūsis, A. Structural and Conductivity Studies in $LiFeP_2O_7$, $LiScP_2O_7$ and $NaScP_2O_7$. *J. Solid State Electrochem.* **2000**, *4*, 146−152.
(20) Hamady, A.; Jouini, T. $NaYP_2O_7$. *Acta Crystallogr.* **1996**, *C52*, 2949−2951.
(21) Yuan, J.; Zhang, H.; Chen, H.; Yang, X.; Zhao, J.; Gu, M. Synthesis, Structure and X-ray Excited Luminescence of Ce^{3+}-Doped $AREP_2O_7$-Type Alkali Rare Earth Diphosphates (A = Na, K, Rb, Cs; RE = Y, Lu). *J. Solid State Chem.* **2007**, *180*, 3381−3387.
(22) Khay, N.; Ennaciri, A.; Harcharras, M. Vibrational Spectra of Double Diphosphates $RbLnP_2O_7$ (Ln = Dy, Ho, Y, Er, Tm, Yb). *Vib. Spectrosc.* **2001**, *27*, 119−126.
(23) Tie, S.-L.; Li, Y.-Y.; Yang, Y. Structure and Vibration Spectra of New Pseudo-Pyrophosphate $NaDyP_2O_7$. *J. Phys. Chem. Solids* **1997**, *58*, 957−961.
(24) Shannon, R. D. Revised Effective Ionic Radii and Systematic Studies of Interatomic Distances in Halides and Chalcogenides. *Acta Crystallogr., Sect. A: Cryst. Phys., Diffr., Theor. Gen. Crystallogr.* **1976**, *A32*, 751−767.
(25) Ng, H. N.; Calvo, C. The Crystal Structure of $KAlP_2O_7$. *Can. J. Chem.* **1973**, *51*, 2613−2620.
(26) Gabelica-Robert, M.; Goreaud, M.; Labbe, P.; Raveau, B. The Pyrophosphate $NaFeP_2O_7$: A Cage Structure. *J. Solid State Chem.* **1982**, *45*, 389−395.
(27) Nasri, S.; Megdiche, M.; Gargouri, M. DC conductivity and study of AC electrical conduction mechanisms by non-overlapping small polaron tunneling model in $LiFeP_2O_7$ ceramic. *Ceram. Int.* **2016**, *42*, 943−951.
(28) Leclaire, A.; Benmoussa, A.; Borel, M. M.; Grandin, A.; Raveau, B. Two Forms of Sodium Titanium(III) Diphosphate: α-$NaTiP_2O_7$ Closely Related to β-cristobalite and β-$NaTiP_2O_7$ Isotypic with $NaFeP_2O_7$. *J. Solid State Chem.* **1988**, *77*, 299−305.
(29) Hamady, A.; Zid, M. F.; Jouini, T. Crystal Structure of KYP_2O_7. *J. Solid State Chem.* **1994**, *113*, 120−124.
(30) Férid, M.; Horchani-Naifer, K. Synthesis, Crystal Structure and Vibrational Spectra of a New Form of Diphosphate $NaLaP_2O_7$. *Mater. Res. Bull.* **2004**, *39*, 2209−2217.
(31) Kiselyova, N. N.; Stolyarenko, A. V.; Ryazanov, V. V.; Sen'ko, O. V.; Dokukin, A. A. Prediction of New $A^{+}B^{+3}X_2^{+5}O_7$ Compounds. *Russ. J. Inorg. Chem.* **2018**, *63*, 1333−1339.
(32) Errandonea, D.; Manjón, F. J. Pressure Effects on the Structural and Electronic Properties of ABX_4 Scintillating Crystals. *Prog. Mater. Sci.* **2008**, *53*, 711−773.
(33) Cakmak, G.; Nuss, J.; Jansen, M. LiB_6O_9F, the First Lithium Flurooxoborate-Crystal Structure and Ionic Conductivity. *Z. Anorg. Allg. Chem.* **2009**, *635*, 631−636.
(34) Ateba Mba, J.-M.; Masquelier, C.; Suard, E.; Croguennec, L. Synthesis and Crystallographic Study of Homeotypic $LiVPO_4F$ and $LiVPO_4O$. *Chem. Mater.* **2012**, *24*, 1223−1234.
(35) Sharp, P. M.; Dyer, M. S.; Darling, G. R.; Claridge, J. B.; Rosseinsky, M. J. Chemically Directed Structure Evolution for Crystal Structure Prediction. *Phys. Chem. Chem. Phys.* **2020**, *22*, 18205.
(36) Wales, D.; Doye, P. K. Global Optimization by Basin-Hopping and the Lowest Energy Structures of Lennard-Jones Clusters Containing up to 110 Atoms. *J. Phys. Chem. A* **1997**, *101*, 5111−5116.
(37) Ong, S. P.; Wang, L.; Kang, B. W.; Ceder, G. Li-Fe-P-O_2 Phase Diagram from First Principles Calculations. *Chem. Mater.* **2008**, *20*, 1798−1807.
(38) Kresse, G.; Furthmüller, J. Efficiency of Ab-initio Total Energy Calculations for Metals and Semiconductors Using a Plane-Wave Basis Set. *Comput. Mater. Sci.* **1996**, *6*, 15−50.
(39) Kresse, G.; Furthmüller, J. Efficient Iterative Schemes For Ab Initio Total-Energy Calculations Using a Plane-Wave Basis Set. *Phys. Rev. B: Condens. Matter Mater. Phys.* **1996**, *54*, 11169−11186.
(40) Sun, J.; Ruzsinszky, A.; Perdew, J. P. Strongly Constrained and Appropriately Normed Semilocal Density Functional. *Phys. Rev. Lett.* **2015**, *115*, 36402.
(41) Sun, J.; Remsing, R. C.; Zhang, Y.; Sun, Z.; Ruzsinszky, A.; Peng, H.; Yang, Z.; Paul, A.; Waghmare, U.; Wu, X.; Klein, M. L.; Perdew, J. P. Accurate First-Principles Structures and Energies of Diversely Bonded Systems from an Efficient Density Functional. *Nat. Chem.* **2016**, *8*, 831−836.
(42) Kitchaev, D. A.; Peng, H.; Liu, Y.; Sun, J.; Perdew, J. P.; Ceder, G. Energetics of MnO_2 Polymorphs in Density Functional Theory. *Phys. Rev. B: Condens. Matter Mater. Phys.* **2016**, *93*, 45132.
(43) Monkhorst, H. J.; Pack, J. D. Special Points for Brillouin-Zone Integrations. *Phys. Rev. B* **1976**, *13*, 5188−5192.
(44) Ong, S. Y.; Richards, W. D.; Jain, A.; Hautier, G.; Kocher, M.; Cholia, S.; Gunter, D.; Chevrier, V. L.; Persson, K. A.; Ceder, G. Python Materials Genomics (Pymatgen): A Robust, Open-Source Python Library for Materials Analysis. *Comput. Mater. Sci.* **2013**, *68*, 314−319.
(45) Li, L.; Chen, Z.; Zhang, Q.; Xu, M.; Zhou, X.; Zhu, H.; Zhang, K. A Hydrolysis-Hydrothermal Route for the Synthesis of Ultrathin

https://doi.org/10.1021/acs.inorgchem.1c01396
Inorg. Chem. XXXX, XXX, XXX−XXX

$LiAlO_2$-inlaid $LiNi_{0.5}Co_{0.2}Mn_{0.3}O_2$ as a High-Performance Cathode Material for Lithium Ion Batteries. *J. Mater. Chem. A* **2015**, *3*, 894−904.
(46) Brown, I. D. Recent Developments in the Methods and Applications of the Bond Valence Model. *Chem. Rev.* **2009**, *109*, 6858−6919.
(47) Xiao, R.; Li, H.; Chen, L. High-Throughput Design and Optimization of Fast Lithium Ion Conductors by the Combination of Bond-Valence Method and Density Functional Theory. *Sci. Rep.* **2015**, *5*, 14227.
(48) Coelho, A. A. TOPAS and TOPAS-Academic: An Optimization Program Integrating Computer Algebra and Crystallographic Objects Written in C++. *J. Appl. Crystallogr.* **2018**, *51*, 210−218.
(49) *SAINT*, version 7.60A; Bruker, 2008.
(50) *SADABS*, version 2008/1; Bruker, 2008.
(51) Sheldrick, G. M. SHELXT-Integrated Space-group and Crystal-structure Determination. *Acta Crystallogr., Sect. A: Found. Adv.* **2015**, *71*, 3−8.
(52) Dolomanov, O. V.; Bourhis, L. J.; Gildea, R. J.; Howard, J. A.; Puschmann, H. OLEX2: A Complete Structure Solution, Refinement and Analysis Program. *J. Appl. Crystallogr.* **2009**, *42*, 339−341.
(53) Sheldrick, G. M. Crystal Structure Refinement with SHELXL. *Acta Crystallogr., Sect. C: Struct. Chem.* **2015**, *C71*, 3−8.
(54) Spek, A. Single-crystal Structure Validation with the Program PLATON. *J. Appl. Crystallogr.* **2003**, *36*, 7−13.
(55) *Zview*, version 3.3f; Scribner Associates Inc., 2016.
(56) Bielecki, A.; Burum, D. P. Temperature Dependence of ^{207}Pb MAS Spectra of Solid Lead Nitrate. An Accurate, Sensitive Thermometer for Variable-Temperature MAS. *J. Magn. Reson., Ser. A* **1995**, *116*, 215−220.
(57) Beckmann, P. A.; Dybowski, C. A Thermometer for Nonspinning Solid-State NMR Spectroscopy. *J. Magn. Reson.* **2000**, *146*, 379−380.
(58) Becker, K. D. Temperature Dependence of NMR Chemical Shifts in Cuprous Halides. *J. Chem. Phys.* **1978**, *68*, 3785−3793.
(59) Wu, J.; Kim, N.; Stebbins, J. F. Temperature Calibration for High-Temperature MAS NMR to 913 K: ^{63}Cu MAS NMR of CuBr and CuI, and ^{23}Na MAS NMR of $NaNbO_3$. *Solid State Nucl. Magn. Reson.* **2011**, *40*, 45−50.
(60) Brese, N. E.; O'Keeffe, M. Bond-Valence Parameters for Solids. *Acta Crystallogr., Sect. B: Struct. Sci.* **1991**, *B47*, 192−197.
(61) Brown, I. D.; Altermatt, D. Bond-Valence Parameters from a Systematic Analysis of the Inorganic Crystal Structure Database. *Acta Crystallogr., Sect. B: Struct. Sci.* **1985**, *B41*, 244−247.
(62) Taher, Y. B.; Oueslati, A.; Khirouni, K.; Gargouri, M. Impedance Spectroscopy and Conduction Mechanism of $LiAlP_2O_7$ Material. *Mater. Res. Bull.* **2016**, *78*, 148−157.
(63) Pachoud, E.; Zhang, W. G.; Tapp, J.; Liang, K. C.; Lorenz, B.; Chu, P.; Halasyamani, P. S. Top-Seeded Single-Crystal Growth, Structure, and Physical Properties of Polar $LiCrP_2O_7$. *Cryst. Growth Des.* **2013**, *13*, 5473−5480.
(64) Ivashkevich, L. S.; Selevich, K. A.; Lenikovich, A. I.; Felevich, A. F. X-ray Powder Diffraction Study of $LiCrP_2O_7$. *Acta Crystallogr.* **2007**, *E63*, 70−72.
(65) Li, Y.; Liang, F.; Song, H.; Liu, W.; Lin, Z.; Zhang, G.; Wu, Y. $LiGaP_2O_7$: A Potential UV Nonlinear-Optical Crystal. *Inorg. Chem.* **2019**, *58*, 6597−6600.
(66) Raguz, B.; Wittich, K.; Glaum, R. Two New, Metastable Polymorphs of Lithium Pyrophosphate $Li_4P_2O_7$. *Eur. J. Inorg. Chem.* **2019**, *11*, 1688−1696.
(67) Voronin, V. I.; Sherstobitova, E. A.; Blatov, V. A.; Shekhtman, G. Sh Lithium-Cation Conductivity and Crystal Structure of Lithium Diphosphate. *J. Solid State Chem.* **2014**, *211*, 170−175.
(68) Lapshin, A. E.; Petrova, M. A. Mixed Alkali-Zinc Diphosphates: Synthesis, Structure, and Properties. *Glass Phys. Chem.* **2012**, *38*, 491−503.
(69) Petrova, M. A.; Petrov, S. A.; Sinel'shchikova, O. Y.; Popova, V. F.; Ugolkov, V. L. Electroconductivity of Alkali-Zinc Diphosphates in Partial Sections of the $Zn_2P_2O_7$-$Li_2ZnP_2O_7$-$Na_2ZnP_2O_7$-$K_2ZnP_2O_7$ System. *Glass Phys. Chem.* **2015**, *41*, 528−532.
(70) Gao, J. H.; Sha, X. S.; Song, L. M.; Zhao, P.; Liu, X. The Synthesis, Structure and Properties of a New Lithium-Rich Manganese(II) Phosphate $Li_5CsMn(P_2O_7)_2$: a Congruently Melting Compound with a Lithium Hamburger Structure. *Dalton Trans.* **2016**, *45*, 2584.
(71) Sun, W.; Dacek, S. T.; Ong, S. P.; Hautier, G.; Jain, A.; Richards, W. D.; Gamst, A. C.; Persson, K. A.; Ceder, G. The Thermodynamic Scale of Inorganic Crystalline Metastability. *Sci. Adv.* **2016**, *2*, No. e1600225.
(72) Zhang, Y.; Kitchaev, D. A.; Yang, J.; Chen, T.; Dacek, S. T.; Sarmiento-Pérez, R. A.; Marques, M. A. L.; Peng, H.; Ceder, G.; Perdew, J. P.; Sun, J. Efficient First-Principles Prediction of Solid Stability: Towards Chemical Accuracy. *npj Comput. Mater.* **2018**, *4*, 9.
(73) Cui, Z. H.; Wu, F.; Jiang, H. First-Principles Study of Relative Stability of Rutile and Anatase TiO_2 Using the Random Phase Approximation. *Phys. Chem. Chem. Phys.* **2016**, *18*, 29914−29922.
(74) Barpanda, P.; Liu, G.; Ling, C. D.; Tamaru, M.; Avdeev, M.; Chung, S. C.; Yamada, Y.; Yamada, A. $Na_2FeP_2O_7$: A Safe Cathode for Rechargeable Sodium-Ion Batteries. *Chem. Mater.* **2013**, *25*, 3480−3487.
(75) Kim, H.; Park, C. S.; Choi, J. W.; Jung, Y. Defect-Controlled Formation of Triclinic $Na_2CoP_2O_7$ for 4 V Sodium-Ion Batteries. *Angew. Chem., Int. Ed.* **2016**, *55*, 6662−6666.
(76) Sun, W.; Du, J. Structural Stability, Electronic and Thermodynamic Properties of $VOPO_4$ Polymorphs from DFT+U Calculations. *Comput. Mater. Sci.* **2017**, *126*, 326−335.
(77) Leclercq, B.; Kabbour, H.; Arevalo-Lopez, A.; Huvé, M.; Daviero-Minaud, S.; Minaud, C.; Blazquez Alcover, I.; Mentré, O. Polymorphs, Phase Transitions and Stability in $BaM_2(PO_4)_2$ M = Mn, Fe, Co Systems. *Inorg. Chem. Front.* **2020**, *7*, 239−246.
(78) Minakshi, M.; Mitchell, D.; Jones, R.; Alenazey, F.; Watcharatharapong, T.; Chakraborty, S.; Ahuja, R. Synthesis, Structural and Electrochemical Properties of Sodium Nickel Phosphate for Energy Storage Devices. *Nanoscale* **2016**, *8*, 11291−11305.
(79) Saritas, K.; Krogel, J. T.; Reboredo, F. A. Relative Energies and Electronic Structures of CoO Polymorphs through ab Initio Diffusion Quantum Monte Carlo. *Phys. Rev. B: Condens. Matter Mater. Phys.* **2018**, *98*, 155130.
(80) Saritas, K.; Krogel, J. T.; Kent, P. R. C.; Reboredo, F. A. Diffusion Monte Carlo: A Pathway towards an Accurate Theoretical Description of Manganese Oxides. *Phys. Rev. Mater.* **2018**, *2*, 085801.
(81) Adler, R.; Kang, C. J.; Yee, C. H.; Kotliar, G. Correlated Materials Design: Prospects and Challenges. *Rep. Prog. Phys.* **2019**, *82*, 012504.
(82) Schleife, A.; Fuchs, F.; Furthmüller, J.; Bechstedt, F. First-Principles Study of Ground- and Excited-State Properties of MgO, ZnO and CdO Polymorphs. *Phys. Rev. B: Condens. Matter Mater. Phys.* **2006**, *73*, 245212.
(83) Peintinger, M. F.; Kratz, M. J.; Bredow, T. Quantum-Chemical Study of Stable, Meta-Stable and High-Pressure Alumina Polymorphs and Aluminium Hydroxides. *J. Mater. Chem. A* **2014**, *2*, 13143−13158.
(84) Dove, M. T. Theory of Displacive Phase Transitions in Minerals. *Am. Mineral.* **1997**, *82*, 213−244.
(85) Bianchini, F.; Fjellvåg, H.; Vajeeston, P. Non-hexagonal Na Sublattice Reconstruction in the Super-Ionic Conductor $Na_2Zn_2TeO_6$: Insights from ab Initio Molecular Dynamics. *J. Phys. Chem. C* **2019**, *123*, 4654−4663.
(86) Lapshin, A. E.; Petrova, M. A. Synthesis and Crystal Structure of the Low-Temperature Modification of $Li_{12}Zn_4(P_2O_7)_5$. *Glass Phys. Chem.* **2010**, *36*, 75−79.
(87) Catti, M.; Comotti, A.; Di Blas, S. High-Temperature Lithium Mobility in α-$LiZr_2(PO_4)_3$ NASICON by Neutron Diffraction. *Chem. Mater.* **2003**, *15*, 1628−1632.

https://doi.org/10.1021/acs.inorgchem.1c01396
Inorg. Chem. XXXX, XXX, XXX−XXX

(88) Sudreau, F.; Petit, D.; Boilot, J. P. Dimorphism, Phase Transitions and Transport Properties in $LiZr_2(PO_4)_3$. *J. Solid State Chem.* **1989**, *83*, 78−90.
(89) Ettis, H.; Naili, H.; Mhiri, T. The Crystal Structure, Thermal Behaviour and Ionic Conductivity of a Novel Lithium Gadolinium Polyphosphate $LiGd(PO_3)_4$. *J. Solid State Chem.* **2006**, *179*, 3107−3113.
(90) Kim, S. C.; Lee, M. S.; Kang, J. Y.; Kim, Y. I.; Kim, S. J. Crystal Structure and Ion Conductivity of a New Mixed Anion Phosphate $LiMg_3(PO_4)P_2O_7$. *J. Solid State Chem.* **2015**, *225*, 335−339.
(91) Attfield, J. P. Phosphates. *Encyclopedia of Materials: Science and Technology Second Edition.* **2001**, 6896−6901.
(92) Shang, X. F.; Hiroyoshi, N.; Shigehi, M.; Peng, X.; Masaki, M.; Yasuo, T.; Osamu, Y.; Nobuyuki, I. High Lithium-Ion-Conducting NASICON-Type $Li_{1+x}Al_xGe_yTi_{2-x-y}(PO_4)_3$ Solid Electrolyte. *Front. Energy Res.* **2016**, *4*, 12.
(93) Lang, B.; Ziebarth, B.; Elsasser, C. Lithium Ion Conduction in $LiTi_2(PO_4)_3$ and Related Compounds Based on the NASICON Structure: A First-Principles Study. *Chem. Mater.* **2015**, *27*, 5040−5048.
(94) Kataoka, K.; Nagata, H.; Akimoto, J. Lithium-ion Conducting Oxide Single Crystal as Solid Electrolyte for Advanced Lithium Battery Application. *Sci. Rep.* **2018**, *8*, 9965.

https://doi.org/10.1021/acs.inorgchem.1c01396
Inorg. Chem. XXXX, XXX, XXX−XXX